Available online at www.sciencedirect.com
ScienceDirect
Trans. Nonferrous Met. Soc. China 33(2023) 2014−2029
Transactions of Nonferrous Metals Society of China
www.tnmsc.cn

# Corrosion and discharge behavior of Mg−Zn−Mn−Nd alloys as primary Mg−air batteries anode

De-yu DING, Yu-hang DU, Mei-fang TANG, Bo SONG, Ning GUO, Hong-ju ZHANG, Sheng-feng GUO

Analytical & Testing Center, School of Materials and Energy, Southwest University, Chongqing 400715, China

Received 2 March 2022; accepted 26 April 2022

**Abstract:** The optical microscopy, X-ray diffraction, scanning electron microscopy equipped with energy dispersive spectrometry, electrochemical tests and galvanostatic discharge tests were employed to characterize the microstructure, corrosion resistance and discharge performance of the as-extruded and solution-aged Mg−6Zn−Mn−*x*Nd (ZM61, *x*=0, 0.2, 0.6, 0.8, 1.0, wt.%) alloys. The results indicate that the micro-alloying with Nd can promote the grain refinement of ZM61 alloys, and the as-extruded and solution-aged ZM61−0.6Nd alloys have the best corrosion resistance and discharge performance. However, the heat treatment deteriorates the comprehensive performance of as-extruded alloys. Among all the investigated alloys, the corrosion current density of the as-extruded ZM61−0.6Nd alloy is $1.611\times10^{-5}$ A/cm$^2$, and the discharge potentials are −1.517 and −1.336 V vs SCE at current density of 1 and 10 mA/cm$^2$, respectively, during long-time discharge up to 24 h with the anode efficiency of above 36%, which shows the best comprehensive performance. The good discharge performance can be attributed to the improvement of corrosion resistance and cracking effect of the discharge products.

**Key words:** Mg−6Zn−Mn alloy; Nd addition; Mg−air battery; self-corrosion; discharge performance

## 1 Introduction

At present, the energy used in the world mainly comes from the fossil energy. However, fossil energy will eventually face exhaustion and the ensuing consequent environmental pollution seriously restricts social development. Therefore, it is urgent to develop green energy to replace the fossil energy. Batteries as clean energy source are good substitutes for fossil energy. The primary batteries usually have much higher theoretical energy density than the secondary batteries [1]. Therefore, the primary metal−air batteries have received widespread attention from society in recent years.

Among all the anode materials of primary batteries, Mg exhibits an excellent performance due to its beneficial recovery and good electrochemical performance, such as a large capacity (6.8 kW·h/kg [2−4]) and high theoretical voltage (3.1 V [5]). However, the commercial application of Mg−air batteries is very restricted by the following problems: (1) During the discharge process, $Mg(OH)_2$ will be generated on the surface of the metal electrode. The dense discharge products will cover the fresh surface of the electrode [6,7]; (2) Mg alloys always show serious self-corrosion behavior [8,9]. Therefore, there is no doubt that the development of Mg alloys with a controllable surface morphology of discharge products, and weak self-corrosion ability is of great significance for improving the performance of Mg−air batteries.

The micro-alloying treatment of Mg is an available method to improve its discharge performance. For example, Zn can effectively reduce

**Corresponding author:** Hong-ju ZHANG, Tel: +86-23-68250299, E-mail: zhanghongju@swu.edu.cn;
Sheng-feng GUO, Tel: +86-23-68253204, E-mail: sfguo@swu.edu.cn

DOI: 10.1016/S1003-6326(23)66240-5

the adverse effects of Fe, Ni, and other impurities on the corrosion resistance of pure Mg [10], which is beneficial to improving the corrosion resistance of Mg alloys. Therefore, Mg−Zn alloys can be a potential anode for Mg−air batteries. Nevertheless, there is only a little information about the impact of alloying on the discharge performance of Mg−Zn alloys. For example, the influence of different contents of Zn [2] and different Zn/Y ratios [11] on the discharge performance of Mg, and the effect of Y and Zr [12] on the discharge performance of Mg−6Zn alloy, have been investigated. However, all of these alloys show a relatively low discharge voltage. It is critical to improve the discharge voltage of Mg−Zn alloy system.

For Mg−Zn alloy system, the *T*-phase formed by the addition of Nd exhibits a larger negative potential than the Mg matrix, which can be corroded preferentially during the electrochemical reaction [13]. In addition, Mn element can improve the corrosion resistance of Mg−Zn alloy by reducing the impurity content [14−16]. Moreover, the heat treatment of Mg alloys is also a way to increase the corrosion resistance of alloys [17]. These may improve the discharge performance of the alloys. Therefore, the effects of different Nd contents and heat treatment on the corrosion resistance and discharge performance of Mg−6Zn−1Mn−*x*Nd (ZM61−*x*Nd, *x*=0, 0.2, 0.6, 0.8, 1.0, wt.%) alloys as the anode for Mg−air batteries were investigated in this work, which was focused on the differences between the two types of alloys in the as-extruded and solution-aged state. The present work could provide novel insights for the development of high-performance Mg−air batteries anodes.

## 2 Experimental

### 2.1 Experimental materials

The pure Mg, pure Zn, Mg−4.1wt.%Mn master alloy, and Mg−30wt.%Nd master alloy were melted to prepare the as-cast ZM61−*x*Nd (*x*=0, 0.2, 0.6, 0.8, 1.0, wt.%) alloys by using a ZG−00L vacuum induction smelting furnace and inert protective argon (Ar) gas. The chemical composition of ZM61−*x*Nd (*x*=0, 0.2, 0.6, 0.8, 1.0, wt.%) alloys were examined by an X-ray fluorescence spectrometer (Shimadzu, XRF−1800) as given in Table 1. The as-cast alloy ingots were homogenized at 330 ℃ for 16 h and 420 ℃ for 2 h. Next, the homogenized alloy ingots were subjected to hot extruding at 360 ℃ with an extrusion ratio of 25:1. Then, the extruded ingots were solution heat-treated at 420 ℃ for 2 h and cooled in water. After that, the solution ingots were aged at 180 ℃ for 16 h, followed by cooling in water. Finally, the sample was cut into *d*12 mm × 5 mm sheet by wire cutting for the corrosion and discharge tests.

**Table 1** Chemical composition of experimental alloys (wt.%)

| Alloy | Nd | Mn | Zn | Mg |
|---|---|---|---|---|
| Mg−6Zn−Mn | 0 | 0.90 | 6.13 | Bal. |
| Mg−6Zn−Mn−0.2Nd | 0.14 | 0.95 | 5.79 | Bal. |
| Mg−6Zn−Mn−0.6Nd | 0.58 | 1.02 | 6.09 | Bal. |
| Mg−6Zn−Mn−0.8Nd | 0.78 | 0.92 | 5.25 | Bal. |
| Mg−6Zn−Mn−1.0Nd | 1.05 | 0.98 | 5.87 | Bal. |

### 2.2 Microstructure characterization

The phase composition and corrosion products of samples were characterized by X-ray diffraction (XRD, Shimadzu XRD−6100, Cu $K_\alpha$) within the $2\theta$ angle range from 10° to 80°. The microstructure was also observed by scanning electron microscope (SEM, JSM-6610) equipped with an energy dispersive spectrometer. Before the observation, the samples were ground with emery papers up to 2000#, then polished with diamond to remove most of the scratches, and finely etched with the picric acid.

### 2.3 Electrochemical tests

The corrosion behavior was tested in 3.5 wt.% NaCl solution. The saturated calomel electrode and the graphite electrode were used as reference electrodes and auxiliary electrodes, respectively. The open-circuit potential, impedance and anodic polarization curve were carried out by the electrochemical workstation (Corrtest, CS310, China). Before the test, the samples were immersed in the solution for about 20 min to ensure the alloy surface at a stable state. The time of the open-circuit potential test was 6500 s. The frequency of the EIS test was from $10^5$ Hz to $10^{-2}$ Hz. The potential range of the moving point scanning was a relative open circuit from −0.5 to 1.5 V. Each sample was tested at least three times to ensure the repeatability of the experimental results.

### 2.4 Half-cell discharge tests

The half-cell discharge performance of Mg−air batteries with ZM61−*x*Nd alloys as the anode was evaluated by using 3.5 wt.% NaCl solution as the electrolyte, saturated calomel electrode as the reference electrode, and graphite electrode as the auxiliary electrode. The discharge potential at 1−10 mA/cm$^2$ was monitored by the electrochemical workstation (Corrtest, CS310, China). And the anode utilization efficiency ($\eta$, %), specific energy density ($D_E$, mW·h·g$^{-1}$), power density ($D_p$, W·cm$^{-2}$), anode discharge voltage ($E_{anode}$, V) of the materials could be calculated by Eqs. (1)−(5) [8,18−22]:

$$\eta=\left(\frac{W_{theo}}{\Delta W}\right)\times 100\% \tag{1}$$

where $\Delta W$ (g) is the mass loss of the sample during the discharge process, and $W_{theo}$ (g) is the theoretical mass loss during the discharge process. The mass loss $\Delta W$ (g) was measured by weighing the mass of the sample before and after the reaction.

The theoretical mass loss could be calculated by the following formula:

$$W_{theo}=\frac{I\cdot t}{F\sum\left(\frac{x_i\cdot n_i}{m_i}\right)} \tag{2}$$

where $I$ (A) is the discharge current, $t$ (h) is the discharge time, $F$ (26.8 A·h/mol) is the Faraday constant, $x_i$, $n_i$, and $m_i$ are the mass fraction, number of exchanged electrons, and atomic mass of the $i$th alloying element in the materials.

$$D_E=\frac{U\cdot I\cdot t}{\Delta W}/1000 \tag{3}$$

where $U$ (V) is the average potential during the discharge process.

$$E_p=U\cdot J \tag{4}$$

where $J$ (A·cm$^{-2}$) is the applied current density.

$$E_{anode}=E_0-\eta_{ct}-\eta_{diff}-iR \tag{5}$$

where $E_0$ (V) is the open circuit potential, $\eta_{ct}$ (V) is the charge transfer overpotential, $\eta_{diff}$ (V) is the diffusion overpotential caused by the discharge product film, $i$ (A) is the load current, and $R$ (Ω) is the electrolyte resistance between the reference electrode and the polarized anode. And the surface products were removed by the chromic acid solution of 200 g/L with the silver nitrate solution of 10 g/L.

## 3 Results

### 3.1 Microstructure characterization

Figure 1 shows the optical micrographs of the as-extruded ZM61−*x*Nd alloys. The microstructures of the as-extruded alloys are mainly composed of $\alpha$-Mg matrix and the second phases (dark areas). The as-extruded ZM61 alloy exhibits fine equiaxed crystals and some deformed grains (Fig. 1(a)). The grain size is mainly from 3 to 9 μm, indicating that the partial dynamic recrystallization has occurred. With the addition of Nd (0.2 wt.%, see Fig. 1(b)), the alloy presents a mixed structure of the equiaxed grains and more deformed grains (approximately 5% of grains are larger than 18 μm). When the $x$>0.2 (Figs. 1(c, d, e)), the grain of ZM61−*x*Nd alloys is refined significantly and nearly 90% of the grain size of as-extruded ZM61−1.0Nd alloy is less than 6 μm (Fig. 1(e)), implying that the dynamic recrystallization rate of the alloys is increased, which is similar to the effect of Nd on the Mg−Zn−Zr alloy [13]. Figure 2 shows the microstructures of the solution-aged ZM61−*x*Nd consist of $\alpha$-Mg matrix and the second phases (dark areas). In the solution-aged ZM61−*x*Nd alloys, most of the grain sizes are between 3 and 9 μm. And the solution-aged ZM61−0.2Nd alloy contains 4.4% of the grain with size larger than 18 μm (Fig. 2(b)). In addition, nearly 82% of the solution-aged ZM61−1.0Nd alloy grain size is less than 6 μm (Fig. 2(e)). These show that the effect of the addition of Nd element on the grain size of the solution-aged ZM61−*x*Nd alloys is consistent well with that of the as-extruded ZM61−*x*Nd alloys.

Figure 3 shows the XRD patterns of the as-extruded and the solution-aged ZM61−*x*Nd alloys. It can be observed that the as-extruded ZM61 alloy contains $\alpha$-Mg phase and a small amount of $MgZn_2$ phase (Fig. 3(a)). With the addition of Nd element, more $T$-phases precipitate and there is no other phase transformations in the alloy. In addition, the diffraction peak of Mn in all the as-extruded ZM61−*x*Nd alloys indicates the very limited solid solubility of Mn in Mg alloys. For the solution-aged ZM61−*x*Nd alloys (Fig. 3(b)), $\alpha$-Mg phase, $MgZn_2$ phase, $T$-phase and Mn phase also exhibit. This indicates that the solution and aging treatments have a slight effect on the phase

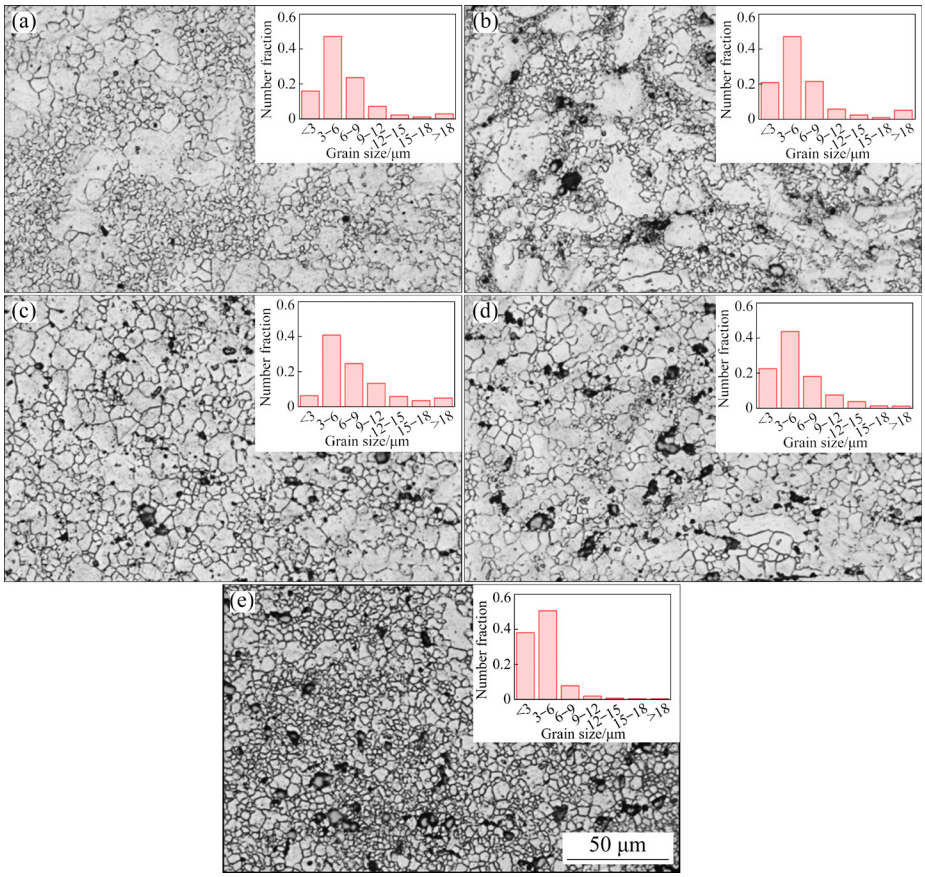


**Fig. 1** Optical microstructures of as-extruded ZM61−*x*Nd alloys: (a) *x*=0; (b) *x*=0.2; (c) *x*=0.6; (d) *x*=0.8; (d) *x*=1.0

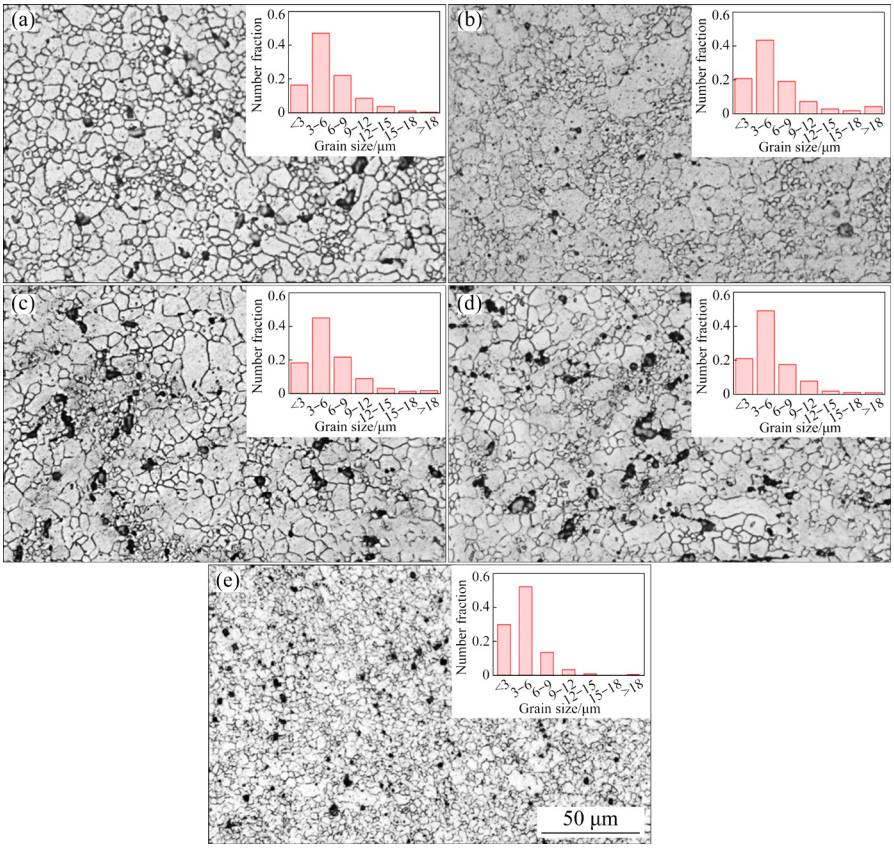


**Fig. 2** Optical microstructures of solution-aged ZM61−*x*Nd alloys: (a) *x*=0; (b) *x*=0.2; (c) *x*=0.6; (d) *x*=0.8; (d) *x*=1.0

composition of ZM61−*x*Nd alloys. And the existence of the *T*-phase also shows that the Nd element has good thermal stability.

The EDS analysis results of the as-extruded ZM61−*x*Nd alloys (see Fig. 4 and Table 2) show that the second phase particles are mainly $MgZn_2$ phases or a mixture of $MgZn_2$ phase with $Mg_{52}Zn_{40}Nd_8$ that belongs to the $T_2$ phase [13]. When the amount of Nd added is very small (<0.2 wt.%), the second phase particles are $MgZn_2$ phases (Fig. 4(a)). With the addition of Nd from 0.2 to 1.0 wt.% (Figs. 4(b−e)), the contents and particle size of the *T*-phase increase significantly. For the as-solution-aged ZM61−*x*Nd alloys (Fig. 5), some small particles distribute on the surface of the Mg matrix, where the enrichment of Zn occurs in ZM61 alloy after the solution and aging treatment (Fig. 5(a)), which correspond to the $MgZn_2$ phase in the XRD pattern. With the addition of Nd (from 0.2 to 1.0 wt.%; Figs. 5(b−e)), the second phase particles also grow significantly. Carefully compared with the as-extruded alloys, the second

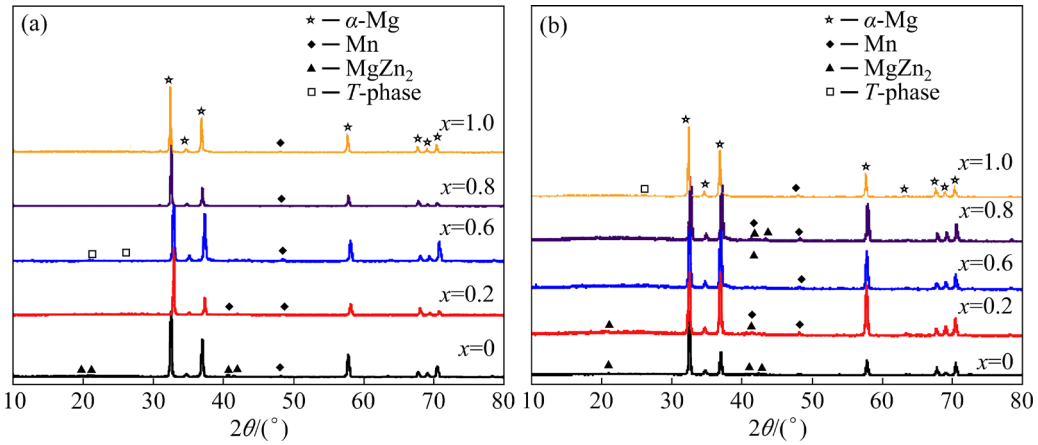


**Fig. 3** XRD patterns of ZM61−*x*Nd alloys: (a) As-extruded; (b) Solution-aged

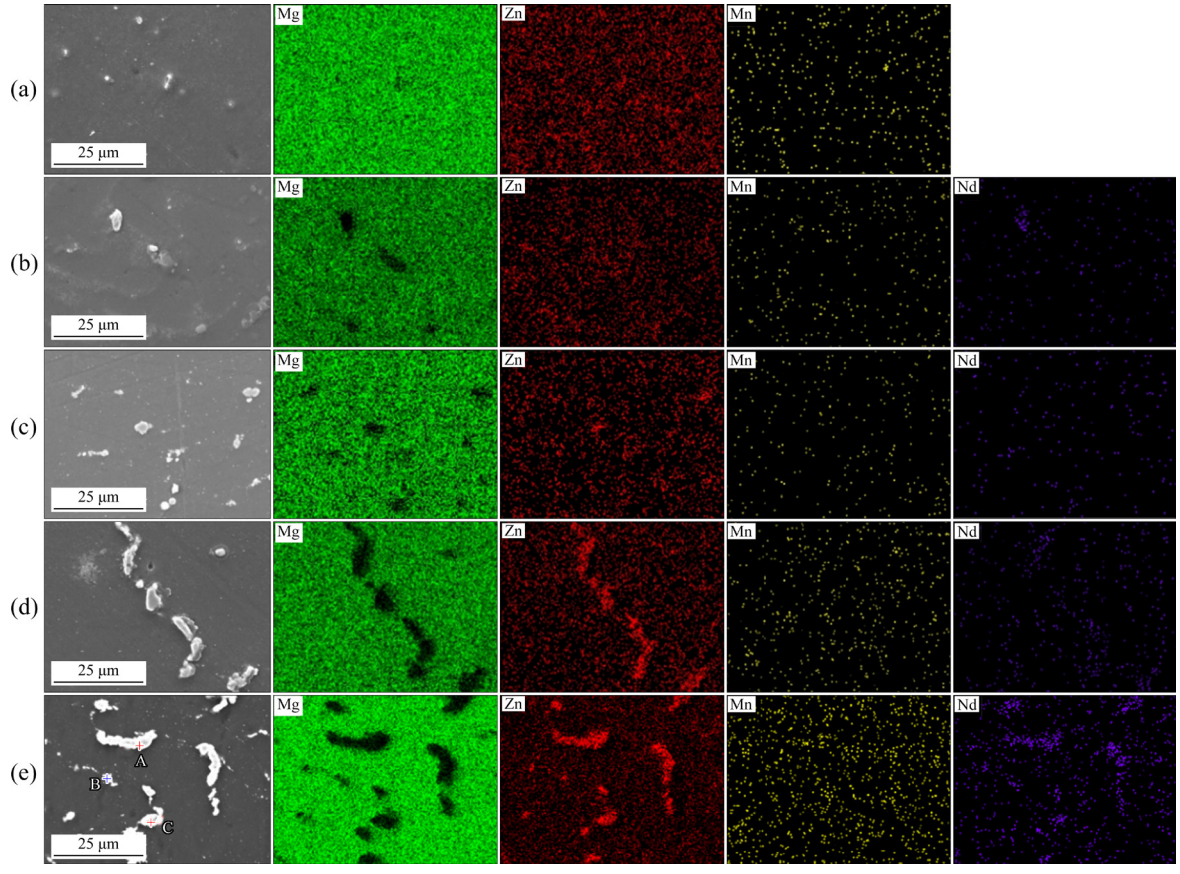


**Fig. 4** EDS mappings of as-extruded ZM61−*x*Nd alloys: (a) *x*=0; (b) *x*=0.2; (c) *x*=0.6; (d) *x*=0.8; (e) *x*=1.0

**Table 2** Elemental composition of Points A, B and C in Fig. 4 (at.%)

| Point | Mg | Zn | Mn | Nd |
|---|---|---|---|---|
| A | 52 | 39.6 | 1.2 | 7.1 |
| B | 78.9 | 18.3 | 0.5 | 2.3 |
| C | 52.7 | 39.6 | 0.7 | 7.1 |

phase particles of the as-solution-aged alloys are considerably coarser.

### 3.2 Electrochemical behaviors

The electrochemical impedance spectroscopy (EIS) technology can be used to study the electrode interface structure and kinetic behavior of the alloys during the corrosion process [23]. The EIS diagrams of the as-extruded and solution-aged ZM61−*x*Nd alloys are shown in Figs. 6(a−f). The Nyquist plots of the as-extruded ZM61−*x*Nd alloys with only one capacitor circuit are similar to those of the solution-aged ZM61−*x*Nd alloys (see Figs. 6(a, b)). The impedance arc is related to the electron transfer and corrosion resistance: the larger the radius of the impedance arc is, the greater the charge transfer resistance is, and the better the corrosion resistance of the materials is. Simultaneously, the phase angle is close to −90°, indicating that the alloys generate a stable corrosion layer on the surface [24,25]. For the as-extruded ZM61−*x*Nd alloys, the radius of the impedance arc decreases in the order of ZM61−0.6Nd > ZM61−0.2Nd > ZM61 > ZM61−0.8Nd > ZM61−1.0Nd. The solution-aged ZM61−*x*Nd alloys show the same trend of the radius of the impedance arc. All the radii of the impedance arc first increase and then decrease with the addition of Nd. The impedance modulus of alloys (Figs. 6(c, d)) reaches the highest peak when 0.6 wt.% Nd is added. The phase angles (about −62°) of as-extruded and solution-aged ZM61−*x*Nd alloys ($x$≤0.8 wt.%) are similar. However, the phase angles (about −57°) of the ZM61−1.0Nd alloy in both states are the highest among the alloys (Figs. 6(e, f)). These indicate that the two types of alloys with 0.6 wt.% Nd addition exhibit the best corrosion resistance. By comparing these alloys, the corrosion resistance of the as-extruded ZM61−*x*Nd alloys is much higher than that of the solution-aged ZM61−*x*Nd alloys.

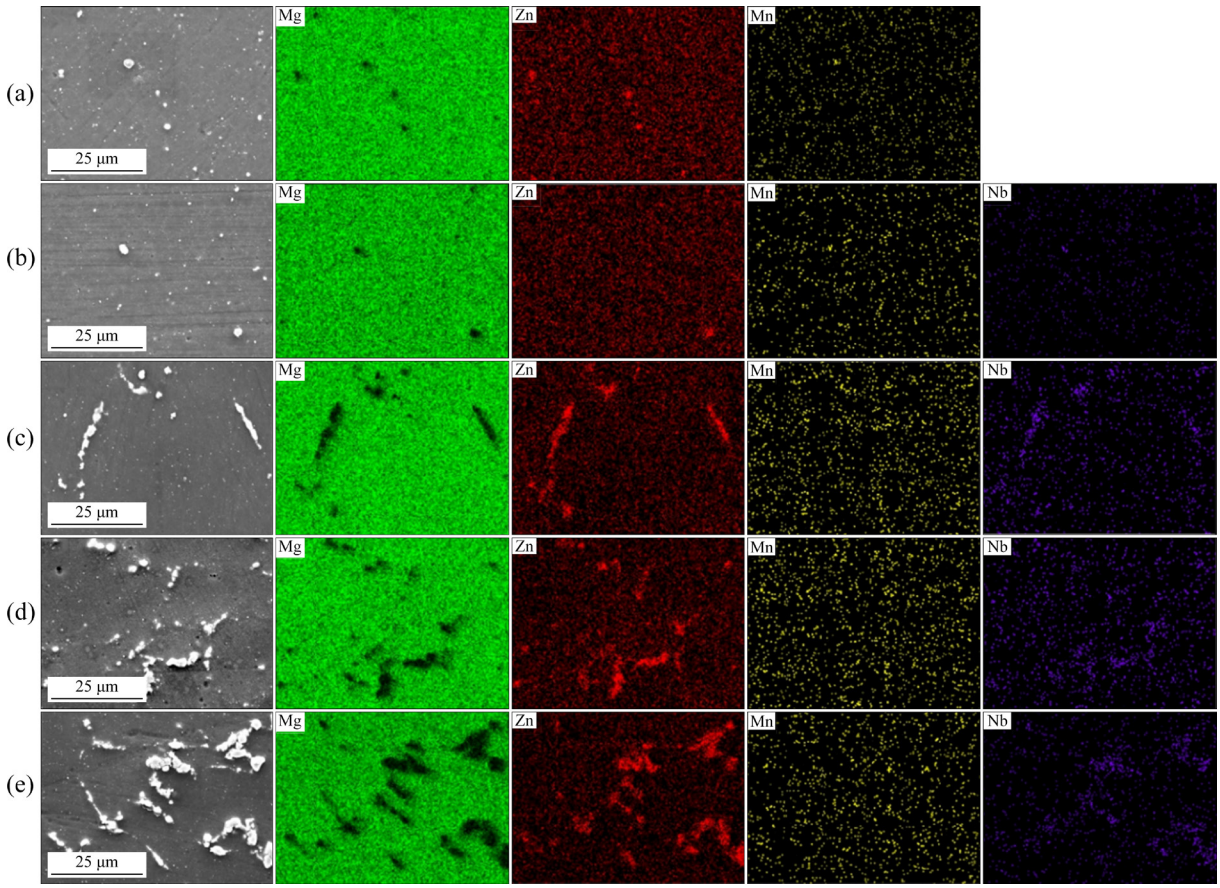


**Fig. 5** EDS mappings of solution-aged ZM61−*x*Nd alloys: (a) $x$=0; (b) $x$=0.2; (c) $x$=0.6; (d) $x$=0.8; (e) $x$=1.0

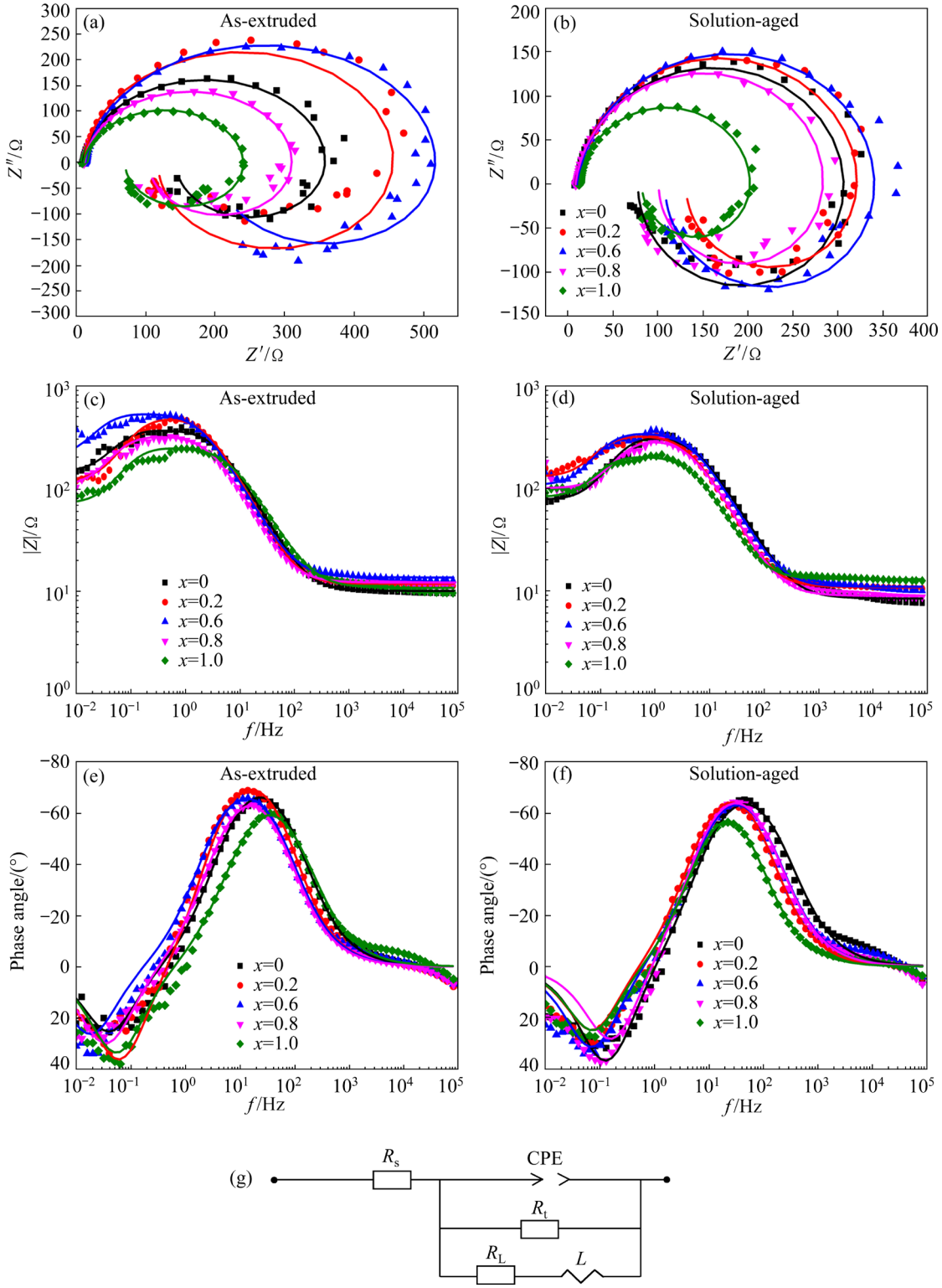


**Fig. 6** EIS diagrams of ZM61−*x*Nd alloys: (a, b) Nyquist diagram; (c, d) Bode diagram of impedance modulus with frequency; (e, f) Bode diagram of phase angle with frequency; (g) Analog circuit

To further study the corrosion mechanism of ZM61−*x*Nd alloys, the equivalent circuit is used to simulate the impedance. The equivalent circuit and its electrochemical parameters are shown in Fig. 6(g) and Table 3, respectively. The $R_s$ is the solution resistance, the CPE is the interface capacitance, the $R_t$ is the interface reaction resistance, and the $R_L$ and $L$ are used to describe the inductance loop in the fourth quadrant. The $R_t$ value determines the corrosion resistance of the

material to a certain extent: the larger $R_t$ means the better corrosion resistance of the materials. For the as-extruded ZM61−$x$Nd alloys, the $R_t$ of ZM61−0.6Nd alloy is 514.0 Ω·cm$^2$, while that of ZM61−1.0Nd alloy is only 235.2 Ω·cm$^2$. For the solution-aged ZM61−$x$Nd alloys, the $R_t$ value of ZM61−0.6Nd alloy is 339.2 Ω·cm$^2$, and that of ZM61−1.0Nd alloy is only 193.9 Ω·cm$^2$. The $R_t$ values of the alloys of the two types of alloys show the same trend of first increasing and then decreasing with the addition of Nd.

Figure 7 shows the polarization curves of the as-extruded ZM61−$x$Nd and solution-aged ZM61−$x$Nd alloys. In the polarization curve, the cathode branch represents the hydrogen evolution reaction, and the anode branch shows the anodic polarization behavior. There is only a slight change of the cathode branch for the tested alloys, indicating that the addition of Nd has no significant effect on the hydrogen evolution reaction of the as-extruded and solution-aged ZM61−$x$Nd alloys. For the anode branch, the curves have the inflection point that may be related to the destruction of the reactive layer on the surface of the sample caused by high current density.

The self-corrosion current density ($J_{corr}$) reflects the corrosion resistance roughly [26], which can be determined by using Tafel extrapolation and summarized in Table 3. For the two types of ZM61−$x$Nd alloys, the $J_{corr}$ shows the same trend with the addition of Nd and decreases in the order of ZM61−1.0Nd > ZM61−0.8Nd > ZM61 > ZM61−0.2Nd > ZM61−0.6Nd. With the addition of Nd, the $J_{corr}$ first decreases and then increases. The as-extruded and solution-aged alloys with 0.6 wt.% Nd have the lowest $J_{corr}$, which are $1.611\times10^{-5}$ A/cm$^2$ (as-extruded ZM61−0.6Nd) and $2.201\times10^{-5}$ A/cm$^2$ (solution-aged ZM61−0.6Nd). The ZM61−0.6Nd alloys show the best corrosion resistance and this agrees well with the EIS results.

**Table 3** Electrochemical parameters of fitted equivalent circuits and corrosion current density of ZM61−$x$Nd alloys

| Material | $R_s$/(Ω·cm$^2$) | $R_t$/(Ω·cm$^2$) | $R_L$/(Ω·cm$^2$) | $L$/H | $J_{corr}$/($10^{-5}$A·cm$^{-2}$) |
|---|---|---|---|---|---|
| Extruded ZM61 | 9.9 | 355.2 | 214.7 | 1332.6 | 1.976 |
| Extruded 0.2Nd | 11.6 | 455.9 | 138.9 | 732.3 | 1.832 |
| Extruded 0.6Nd | 13.5 | 514.0 | 294.7 | 4100 | 1.611 |
| Extruded 0.8Nd | 12.0 | 301.2 | 146.9 | 1063.5 | 2.206 |
| Extruded 1.0Nd | 10.6 | 235.2 | 79.7 | 462.1 | 3.013 |
| Solution-aged ZM61 | 8.6 | 310.8 | 90.1 | 239.3 | 2.333 |
| Solution-aged 0.2Nd | 11.1 | 318.5 | 194.1 | 698.0 | 2.216 |
| Solution-aged 0.6Nd | 11.2 | 339.2 | 136.4 | 578.2 | 2.201 |
| Solution-aged 0.8Nd | 9.3 | 288.1 | 136.0 | 235.8 | 2.851 |
| Solution-aged 1.0Nd | 13.2 | 193.9 | 108.8 | 400.2 | 3.650 |

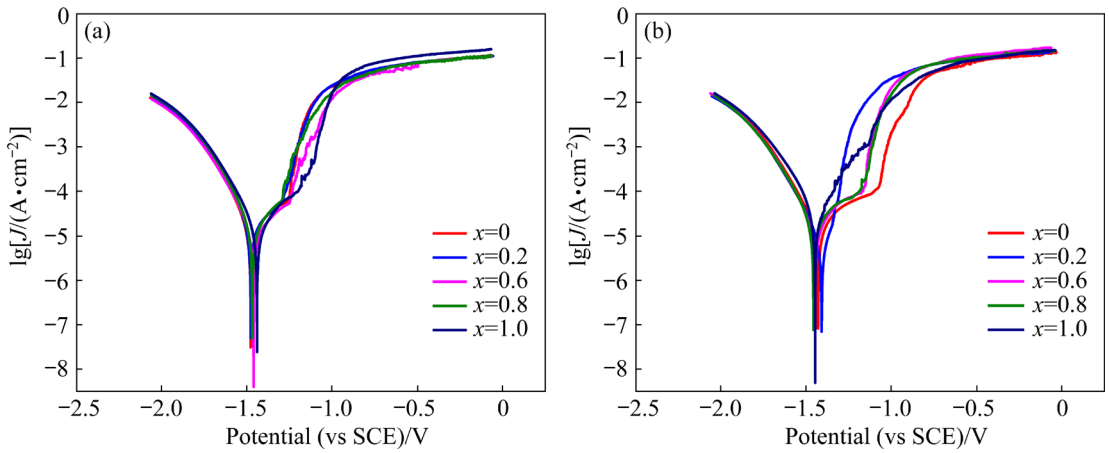


**Fig. 7** Polarization behavior of ZM61−$x$Nd alloys in 3.5 wt.% NaCl solution: (a) As-extruded; (b) Solution-aged

### 3.3 Discharge behavior

The galvanostatic discharge test is usually used to characterize the discharge performance of the materials. The discharge results of the alloys in 3.5 wt.% NaCl solution are shown in Fig. 8.

Figures 8(a−d) display the discharge curves of the as-extruded and solution-aged ZM61−*x*Nd alloys at current density of 1 and 10 mA/cm$^2$. Under the current density of 1 mA/cm$^2$, the as-extruded and the solution-aged ZM61−*x*Nd alloys exhibit the lowest potential when *x*=0.6, which are −1.555 and −1.550 V vs SCE, respectively. Under the current density of 10 mA/cm$^2$, the discharge potential of the as-extruded and the solution-aged ZM61−*x*Nd alloys decrease first and then increase with the addition of Nd. Both of them get the highest value

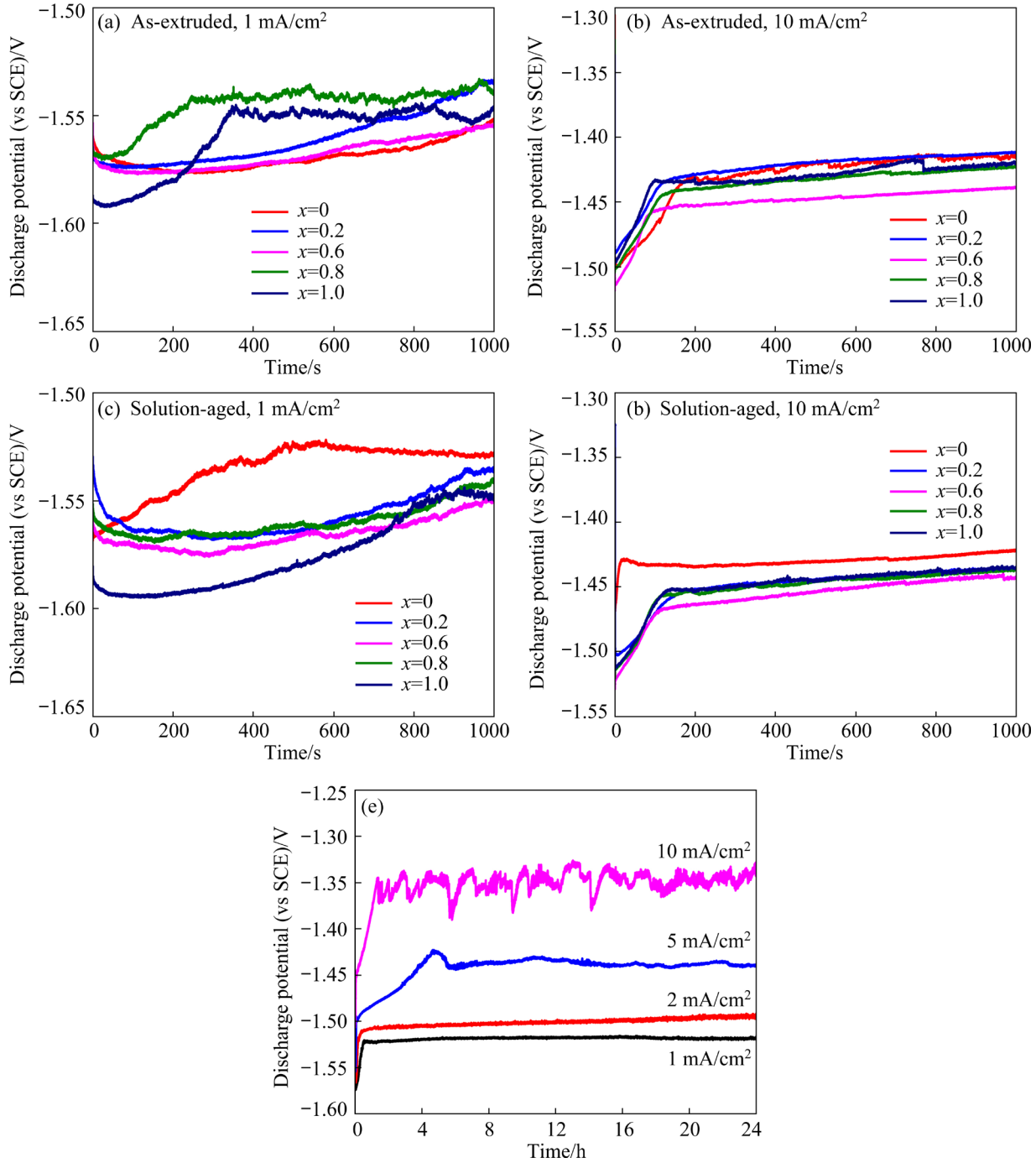


**Fig. 8** Discharge potential−time curves of ZM61−*x*Nd alloys discharged in 3.5 wt.% NaCl solution for 1000 s at current density of 1 and 10 mA/cm$^2$ (a−d), and discharge potential−time curves of as-extruded ZM61−0.6Nd alloy for 24 h (e)

when 0.6 wt.% Nd is added, which are −1.439 and −1.443 V vs SCE, respectively. By comprehensive consideration of the corrosion resistance of tested alloys, the as-extruded ZM61−0.6Nd alloy is chosen as the anode for 24 h galvanostatic discharge test (Fig. 8(e)). The discharge performances of the as-extruded ZM61−0.6Nd alloy are shown in Fig. 9. It can be seen that the discharge potentials and anodic utilization efficiency of the ZM61−0.6Nd alloy as the Mg−air battery anode at 1, 2, 5, 10 mA/cm$^2$ are −1.517 V vs SCE, 35.6%; −1.496 V vs SCE, 32.4%; −1.439 V vs SCE, 31.8%; −1.336 V vs SCE, 35.7%, respectively. The high anodic efficiency for the as-extruded ZM61−0.6Nd alloy is closely related to the low self-corrosion effect of ZM61−Nd alloy. It can be seen from the impedance value that although the as-extruded ZM61−0.6Nd alloy has the highest $R_t$ (514.0 Ω·cm$^2$) among the tested alloys, it has a lower self-corrosion effect during discharge. During half-cell tests, the highest specific energy density is 1187.24 mW·h/g at 1 mA/cm$^2$, the highest power density is 13.36 mW/cm$^2$ at 10 mA/cm$^2$. In addition, the as-extruded ZM61−0.6Nd alloy shows the fluctuations of the discharge potential at 10 mA/cm$^2$, which may be due to the formation and the self-peeling of discharge products. The generation rate of the discharge product is larger than the spalling rate during the discharge process at a high current density, and a large-scale spalling of products occurs at the same time. These would change the active area of the anode dramatically during the discharge process, resulting in fluctuations of discharge potential. In addition, the cathode is also important to increase the properties of Mg anode. Previous researches show that a cathode with high specific surface area and high electrocatalytic performance is beneficial to improving the performance of Mg anode [33,34].

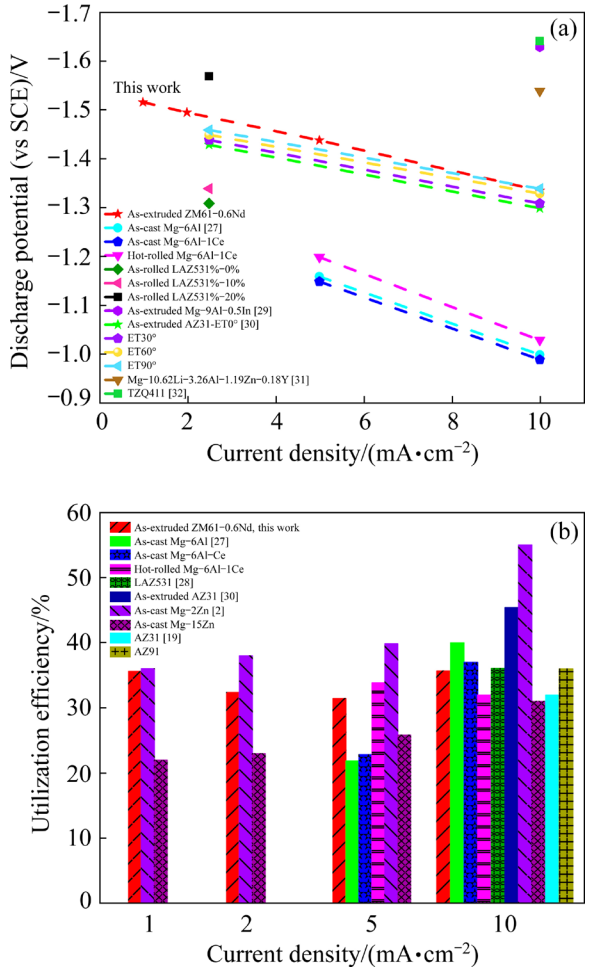


**Fig. 9** Discharge potential (a) and utilization efficiency (b) of Mg alloys at different current densities in 3.5 wt.% NaCl solution [2,27−32]

### 3.4 Surface morphologies after discharge

Figures 10 and 11 show surface morphologies after discharge without any treatment. The surface morphologies of the as-extruded and the solution-aged ZM61 (Figs. 10(a, d)), ZM61−0.6Nd (Figs. 10(b, e)), ZM61−1.0Nd (Figs. 10(c, f)) alloys after being discharged for 1000 s at the current density of 10 mA/cm$^2$ show many cracks distributed on the surface of the discharge product layer. These cracks can become effective channels, which are beneficial for the electrolyte to contact fresh surfaces and ion diffusion. Moreover, the cross-sectional morphologies of the as-extruded ZM61−0.6Nd at different current densities after 24 h discharge are shown in Fig. 11. After discharging at the current density of 1 mA/cm$^2$ (Fig. 11(a)), 2 mA/cm$^2$ (Fig. 11(b)), 5 mA/cm$^2$ (Fig. 11(c)) and 10 mA/cm$^2$ (Fig. 11(d)) for 24 h, the thickness ranges of reaction products which closely attach to the anode surface are 5−80, 12−117, 25−145 and 30−190 μm, respectively. The thickness of the product layers increases with the ascension of the current density, which can be attributed to the release rate of the discharge product being lower than the generation rate of the product under much higher current density. However, the discharge potential of the ZM61−0.6Nd alloy decreases, which is attributed to the thicker discharge layer. In addition, the product

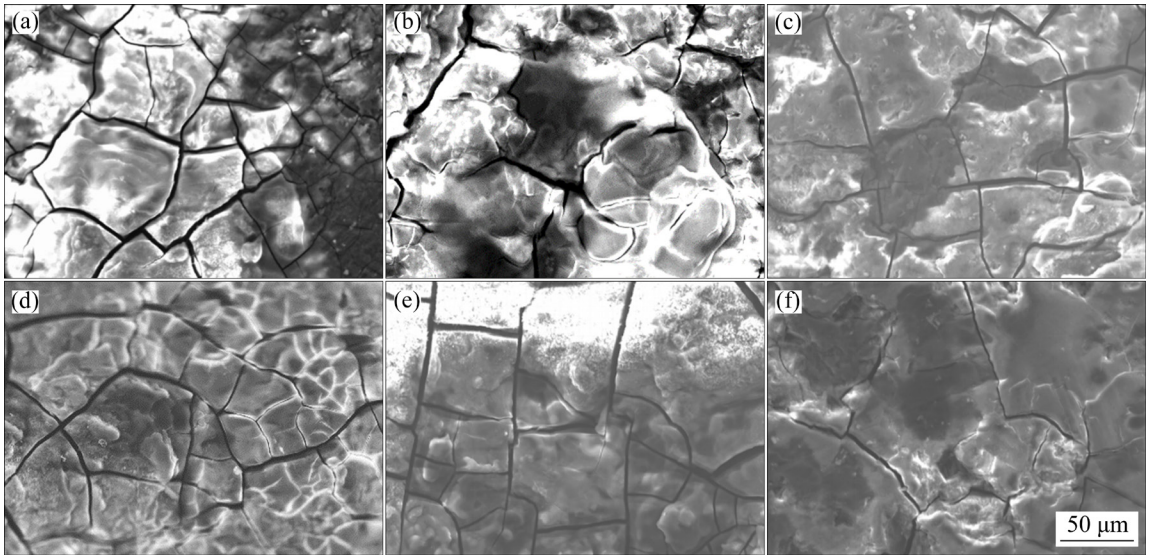


**Fig. 10** SEM images of alloy surface after discharge for 1000 s at current density of 10 mA/cm$^2$: (a) As-extruded ZM61; (b) As-extruded ZM61−0.6Nd; (c) As-extruded ZM61−1.0Nd; (d) Solution-aged ZM61; (e) Solution-aged ZM61−0.6Nd; (f) Solution-aged ZM61−1.0Nd

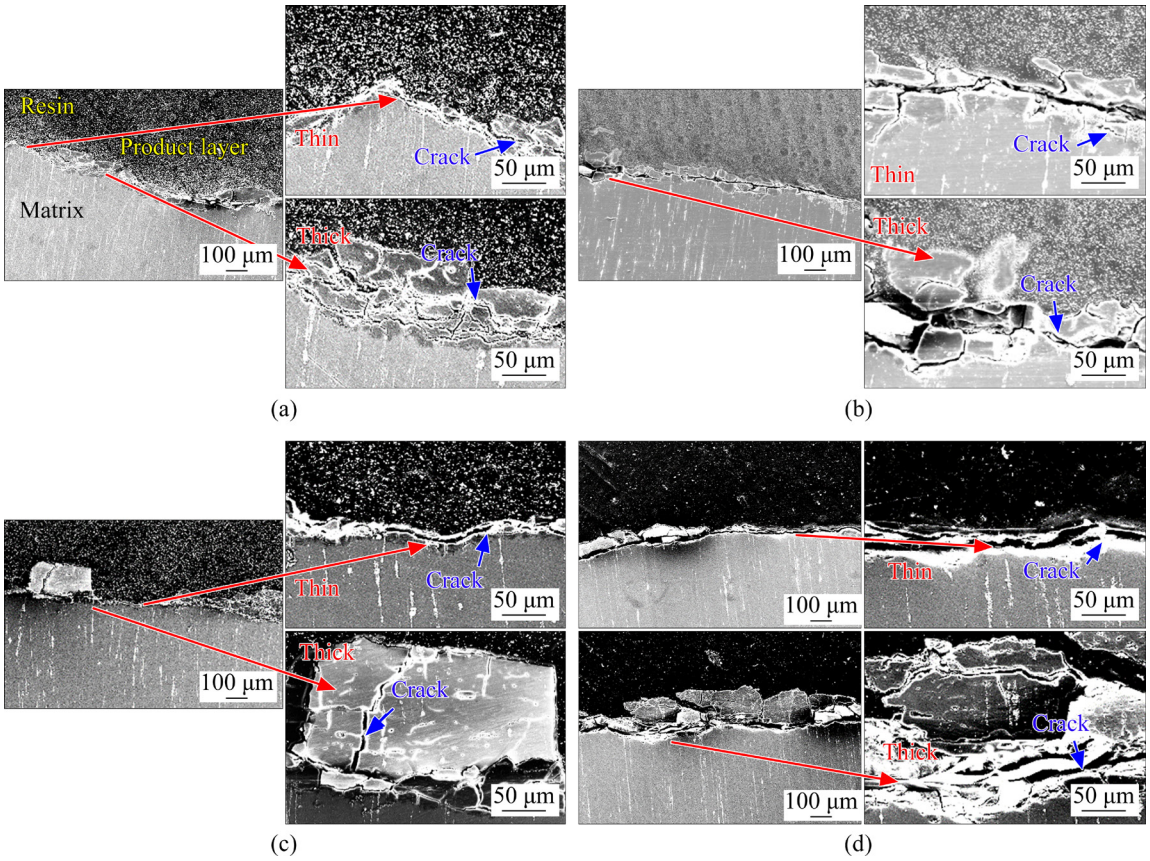


**Fig. 11** SEM images of as-extruded ZM61−0.6Nd with different current densities after 24 h of discharge: (a) 1 mA/cm$^2$; (b) 2 mA/cm$^2$; (c) 5 mA/cm$^2$; (d) 10 mA/cm$^2$

layers are separated from the anode substrate with a lot of cracks, resulting in the electrolyte closely contacted with the anode substrate and conducive to the discharge reaction. The XRD patterns of the discharge products of the ZM61−0.6Nd alloy after discharging for 24 h (Fig. 12) show that the

discharge products are mainly composed of $Mg(OH)_2$ and $Zn(OH)_2$ without pure Mg, implying that the ZM61−0.6Nd alloy completely participates in the reaction during the discharge. This behavior is different from the Mg−0.2Ca−0.4In [35] and Mg−Al−Zn−In [36] alloys in the discharge layer where the unreacted metal Mg appears.

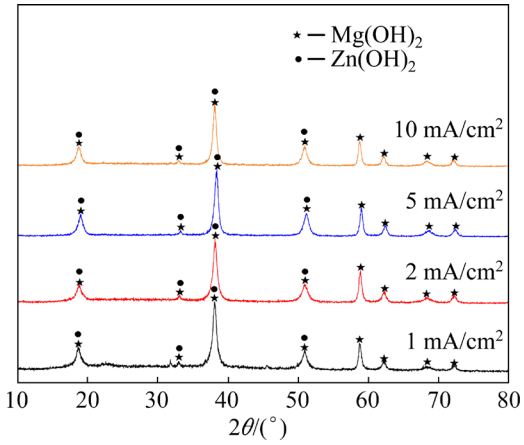


**Fig. 12** XRD patterns of discharge products of as-extruded ZM61−0.6Nd alloy with different current densities

## 4 Discussion

### 4.1 Influence of Nd content on corrosion performance of ZM61 alloys

The addition of Nd promotes the precipitation of the *T*-phase in the as-extruded and solution-aged ZM61 alloy. Therefore, the second phases of the as-extruded and solution-aged ZM61−*x*Nd ($x \geq 0.2$) alloys are mainly composed of $MgZn_2$ and *T*-phase. It should be noticed that the electrode potentials of the $MgZn_2$ phase, Mg matrix and *T*-phase are about −1.01 V vs SCE [37], −1.64 V vs SCE [38], and −2.04 V vs SCE [13], respectively. Therefore, during the corrosion process, the $MgZn_2$ phase acts as the cathode to accelerate the corrosion of the Mg matrix, while the *T*-phase acts as the anode to protect the Mg matrix. With the addition of Nd, the corrosion resistance of the as-extruded and solution-aged ZM61−*x*Nd alloys firstly increases and then decreases. This may be related to the combined effect of the alloy grains and the second phase. Firstly, for the ZM61 alloy with a small amount of Nd (0.2 wt.%), the grain size of the alloy increases, but the precipitated *T*-phase becomes the corrosion anode, which reduces the corrosion rate of the Mg matrix. Secondly, with the addition of Nd from 0.2 to 0.6 wt.%, the grain refinement is significantly manifested and finer *T*-phases are precipitated in the alloys, improving the corrosion resistance of the alloys [39]. When *w*(Nd)>0.6 wt.%, the relatively poor corrosion resistance of the as-extruded and solution-aged alloy may be attributed to the coarse second phase [40]. Therefore, the extruded and solution-aged alloys exhibit the best corrosion resistance when 0.6 wt.% Nd is added. However, the solution-aged ZM61−*x*Nd alloys have a lower corrosion resistance than the as-extruded ZM61−*x*Nd alloys because of the precipitation of coarse *T*-phase after solution-aging treatment.

### 4.2 Influence of Nd content on discharge behavior of ZM61 alloys

The discharge performance of the as-extruded and solution-aged ZM61 alloys firstly increases and then decreases with the addition of Nd, which is attributed to the combined effect of fine grains and self-corrosion. ZHANG et al [41] proposed that if the electrode process of Mg alloys was only activated and controlled without passivation, the grain boundary would accelerate the anodic dissolution rate of Mg alloys. With the addition of Nd, the as-extruded and solution-aged ZM61−*x*Nd alloys contain more grain boundaries. The grain boundaries play as preferential sites for the initial attack under applied anodic current and promote the discharge activities of Mg alloys. When *w*(Nd) > 0.6 wt.%, the discharge performance of the as-extruded and the solution-aged ZM61 alloys begins to decline, which may be related to a galvanic interaction between *α*-Mg and coarse *T*-phase. Therefore, an appropriate amount of Nd can improve the discharge performance of as-extruded and solution-aged ZM61 alloys. However, the solution aging treatment promotes the precipitation of the coarse *T*-phase, which deteriorates the discharge performance of the as-extruded ZM61−*x*Nd alloys.

### 4.3 Influence of discharge products on discharge performance

The discharge performance of anode material is closely related to the formation rate and the precipitation rate of the discharge product [42].

When the precipitation rate is lower than the formation rate, the discharge products will cover the active part of the anode and reduce the effective area of the anode surface, which will eventually decline the discharge performance of anode. The coarse second phase of the as-extruded and the solution-aged ZM61−*x*Nd alloys ($x$>0.6) will accelerate the self-corrosion process, thereby accelerating the accumulation of discharge products on the anode surface. This worsens the discharge performance of the as-extruded and the solution-aged ZM61−*x*Nd alloys. In addition, when the same volume of Mg and Zn convert into $Mg(OH)_2$ and $Zn(OH)_2$, the volume ratio of Mg: $Mg(OH)_2$ is 1:1.78, and that of Zn:$Zn(OH)_2$ is 1:3.56. Therefore, the production of $Mg(OH)_2$ and $Zn(OH)_2$ from the Mg and Zn will cause volume expansion. For the as-extruded and the solution-aged ZM61−*x*Nd alloys, the precipitation phases are mainly *T*-phase and $MgZn_2$ phase. When the as-extruded and the solution-aged ZM61−*x*Nd alloys are used as the anode of the Mg−air batteries, the *T*-phase and $MgZn_2$ phase have disparate effects for the generation of cracks in the discharge product layer. Firstly, the *T*-phase reacts preferentially because of the lower electrode potential than pure Mg during the discharge process. Meanwhile, the volume expansion of *T*-phase is much higher than that of the Mg matrix, which will destroy the discharge product layer by the swelling stress. Moreover, the pining effect of the $MgZn_2$ phase causes the appearance of cracks in the product layer because the electrode potential of $MgZn_2$ phase is much higher the Mg matrix (see Fig. 11). The schematic illustration of the cracks in the discharge product layer is shown in Fig. 13. This is conducive to the electrolyte contacting the anode and exposing a more active surface from the anode, which improves the discharge performance of the materials.

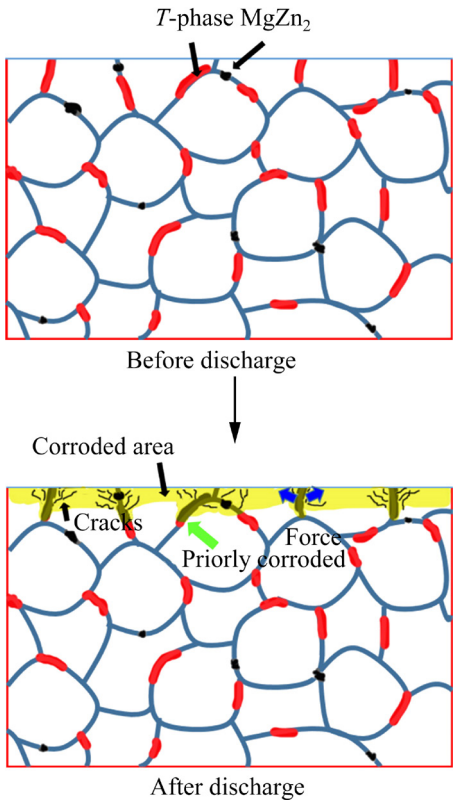


**Fig. 13** Schematic illustration of cracks in discharge product layer

## 5 Conclusions

(1) Micro-alloying Nd can effectively promote the grain refinement and the precipitation of the $T_2$ phase in the as-extruded ZM61 alloy. The solution treatment at 420 ℃ for 2 h and cooled in water, then aged at 180 ℃ for 16 h and cooled in water can promote the growth of the $T_2$ phase.

(2) The combined effect of the $T_2$ phase and fine grains improves the corrosion resistance of ZM61−*x*Nd alloy. However, when $x > 0.6$, ZM61−*x*Nd alloy forms coarse $T_2$ phase, which destroys the corrosion resistance of the alloy.

(3) The as-extruded ZM61−0.6Nd alloy has the best discharge performance among all the alloys tested, and the discharge potentials are −1.517 and −1.336 V vs SCE at current densities of 1 and 10 mA/cm$^2$ for 24 h, respectively, and utilization efficiency is about 36%. The analysis shows that the finer grains and the more negative electrode potential of the $T_2$ phase promote the discharge reaction of the alloy. In addition, the stress from the different volume expansion rates of $Mg(OH)_2$ and $Zn(OH)_2$ promotes the cracking of the discharge product layer during the discharge process. At the same time, the $MgZn_2$ with the correct electrode potential also causes the cracking of the product layer. Therefore, the discharge product layer of the ZM61−*x*Nd alloys is easier to separate from the substrate and the anode fully contacts the electrolyte, resulting in the improvement of the discharge performance.

## Acknowledgments

This work was financially supported by the National Natural Science Foundation of China (No. 52071276) and the Natural Science Foundation of Chongqing City, China (No. cstc2020jcyj-msxmX0933).

## References

[1] CHENG Fang-yi, CHEN Jun. Metal-air batteries: From oxygen reduction electrochemistry to cathode catalysts [J]. Chemical Society Review, 2012, 41: 2172−2192.

[2] TONG Fang-lei, CHEN Xi-ze, WANG Qing, WEI Shang-hai, GAO Wei. Hypoeutectic Mg−Zn binary alloys as anode materials for magnesium−air batteries [J]. Journal of Alloys and Compounds, 2021, 857: 157579.

[3] FENG Yan, LEI Ge, HE Yu-qing, WANG Ri-chu, WANG Xiao-feng. Discharge performance of Mg−Al−Pb−La anode for Mg−air battery [J]. Transactions of Nonferrous Metals Society of China, 2018, 28: 2274−2286.

[4] LI Quan, XIONG Wei, YU Si-rong, LIU Ying, LI Jing, LIU Lin, BI Xiao-jian, ZHU Guang, LIU En-yang, ZHAO Yan, WANG Bing-ying. Effect of Gd content on the discharge and electrochemical behaviors of the magnesium alloy AZ31 as an anode for Mg−air battery [J]. Journal of Materials Science, 2021, 56: 12789−12802.

[5] XIONG, Han-qing, YU Kun, YIN Xiang, DAI Yi-long, YAN Yang, ZHU Hua-long. Effects of microstructure on the electrochemical discharge behavior of Mg−6wt.%Al−1wt.%Sn alloy as anode for Mg−air primary battery [J]. Journal of Alloys and Compounds, 2017, 708: 652−661.

[6] SHRESTHA N, RAJA K S, UTGIKAR V. Mg−RE alloy anode materials for Mg−air battery application [J]. Journal of The Electrochemical Society, 2019, 166: A3139−A3153.

[7] YANG Hua-bao, WU Liang, JIANG Bin, LEI Bin, YUAN Ming, XIE Hong-mei, ATRENS A, SONG Jiang-feng, HUANG Guang-sheng, Pan Fu-sheng. Discharge properties of Mg−Sn−Y alloys as anodes for Mg−air batteries [J]. International Journal of Minerals Metallurgy and Materials, 2021, 28: 1705−1715.

[8] GU Xiong-jie, CHENG Wei-li, CHENG Shi-ming, LIU Yan-hui, WANG Zhi-feng, YU Hui, CUI Ze-qin, WANG Li-fei, WANG Hong-xia. Tailoring the microstructure and improving the discharge properties of dilute Mg−Sn−Mn−Ca alloy as anode for Mg−air battery through homogenization prior to extrusion [J]. Journal of Materials Science & Technology, 2021, 60: 77−89.

[9] CHEN Xing-rui, WANG He-nan, ZOU Qi, LE Qi-chi, WEN Cui-e, ATRENS A. The influence of heat treatment on discharge and electrochemical properties of Mg−Gd−Zn magnesium anode with long period stacking ordered structure for Mg−air battery [J]. Electrochimica Acta, 2021, 367: 137518.

[10] ZHANG Er-lin, YIN Dong-song, XU Li-ping, YANG Lei, YANG Ke. Microstructure, mechanical and corrosion properties and biocompatibility of Mg–Zn–Mn alloys for biomedical application [J]. Materials Science & Engineering C: Materials for Biological Applications, 2009, 28: 987−993.

[11] CHEN Xing-rui, WANG He-nan, LE Qi-chi, JIA Yong-hui, ZHOU Xiong, YU Fu-xiao, ATRENS A. The role of long-period stacking ordered phase on the discharge and electrochemical behaviors of magnesium anode Mg−Zn−Y for the primary Mg−air battery [J]. International Journal of Energy Research, 2020, 44: 8865−8876.

[12] CHEN, Xing-rui, ZOU Qi, LE Qi-chi, HOU Jian, GUO Rui-zhen, WANG He-nan, HU Cheng-lu, BAO Lei, WANG Tong, ZHAO Da-zhi, YU Fu-xiao, ATRENS A. The quasicrystal of Mg−Zn−Y on discharge and electrochemical behaviors as the anode for Mg−air battery [J]. Journal of Power Sources, 2020, 451: 227807.

[13] CAI Chang-hong, SONG Ren-bo, WANG Luan-xiang, LI Jing-yuan. Effect of anodic *T* phase on surface micro-galvanic corrosion of biodegradable Mg−Zn−Zr−Nd alloys [J]. Applied Surface Science, 2018, 462: 243−254.

[14] GU Dong-dong, WANG Jia-wen, Chen Yu-bin, PENG Jian. Effect of Mn addition and refining process on Fe reduction of Mg−Mn alloys made from magnesium scrap [J]. Transactions of Nonferrous Metals Society of China, 2020, 30: 2941−2951.

[15] METALNIKOV P, BEN-HAMU G, TEMPLEMAN Y, SHIN K S, MESHI L. The relation between Mn additions, microstructure and corrosion behavior of new wrought Mg−5Al alloys [J]. Materials Characterization, 2018, 145: 101−115.

[16] HOU Cai-hong, YE Zhi-song, QI Fu-gang, WANG Qing, LI Lian-hui, OUYANG Xiao-ping, ZHAO Nie. Effect of Al addition on microstructure and mechanical properties of Mg−Zn−Sn−Mn alloy [J]. Transactions of Nonferrous Metals Society of China, 2021, 31: 1951−1968.

[17] ZHANG Shao-xiang, LI Jian-an, SONG Yang, ZHAO Chang-li, XIE Chao-ying, ZHANG Xiao-nong. Influence of heat treatments on in vitro degradation behavior of Mg−6Zn alloy studied by electrochemical measurements [J]. Journal of the Mechanical Behavior of Biomedical Materials, 2010, 12: B170−B174.

[18] YUASA M, HUANG Xin-sheng, SUZUKI K, MABUCHI M, CHION Y, Discharge properties of Mg−Al−Mn−Ca and Mg−Al−Mn alloys as anode materials for primary magnesium−air batteries [J]. Journal of Power Sources, 2015, 297: 449−456.

[19] MA Jing-ling, WANG Guang-xin, LI Ya-qiong, REN Feng-zhang, VOLINSKY A A. Electrochemical performance of Mg−air batteries based on AZ series magnesium alloys [J]. Inoics, 2019, 25: 2201−2209.

[20] CHENG Shi-ming, CHENG Wei-li, GU Xiong-jie, YU Hui, WANG Zhi-feng, WANG Hong-xia, WANG Li-fei. Discharge properties of low-alloyed Mg−Bi−Ca alloys as anode materials for Mg−air batteries: Influence of Ca alloying [J]. Journal of Alloys and Compounds, 2020, 823: 153779.

[21] WU Yi-ping, WANG Zhi-feng, LIU Yu, LI Guo-feng, XIE

Shao-hui, YU Hui, XIONG Han-qing. AZ61 and AZ61−La alloys as anodes for Mg−air battery [J]. Journal of Materials Engineering and Performance, 2019, 28: 2006−2016.

[22] NAKAMURA, NISHIKAWA H, AOKI T, OGAMI Y. The diffusion overpotential increase and appearance of overlapping arcs on the Nyquist plots in the low humidity temperature test conditions of polymer electrolyte fuel cell [J], Journal of Power Sources, 2009, 186: 278−285.

[23] ASCENCIO M, PEKGULERYUZ M, OMANOVIC S. Corrosion behaviour of polypyrrole-coated WE43 Mg alloy in a modified simulated body fluid solution [J]. Corrosion Science, 2018, 133: 261−275.

[24] WANG Zhang-bing, HU Hong-xiang, LIU Chun-bo, ZHENG Yu-gui. The effect of fluoride ions on the corrosion behavior of pure titanium in 0.05 M sulfuric acid [J]. Electrochimica Acta, 2014, 135: 526−535.

[25] de ASSIS S L, WOLYNEC S, COSTA I. Corrosion characterization of titanium alloys by electrochemical techniques [J]. Electrochimica Acta, 2006, 51: 1815−1819.

[26] WANG Nai-guang, WANG Ri-chu, PENG Chao-qun, FENG Yan, CHEN Bin. Effect of hot rolling and subsequent annealing on electrochemical discharge behavior of AP65 magnesium alloy as anode for seawater activated battery [J]. Corrosion Science, 2012, 64: 17−27.

[27] SONG Yong-fa, MA Jing-ling, LI Ya-qiong, WANG Guang-xin, QIN Cong-hui, STOCK H R. Effects of second phases in anode materials on discharge performance of Mg−air batteries [J]. Ionics, 2019, 25: 5899−5906.

[28] YANG Hua-bao, WU Liang, JIANG Bin, LEI Bin, LIU Wen-jun, SONG Jiang-feng, ATRENS A, HUANG Guang-sheng, ZHANG Ding-fei, PAN Fu-sheng. Enhancement of corrosion resistance and discharge Performance of Mg−5Li−3Al−1Zn sheet for Mg−air battery via rolling [J]. Journal of the Electrochemical Society, 2020, 167: 110529.

[29] LI Zi-yan, WANG Hong-xia, LI Jun-jian, ZHUANG Yong-peng, GAO Jian-zhong, LI Hang, CHENG Wei-li. Synergistic effect of second phase and grain size on electrochemical discharge performance of extruded Mg−9Al−*x*In alloys as anodes for Mg−air battery [J]. Advanced Engineering Materials, 2020, 22: 1901332.

[30] YANG Hua-bao, LEI Bin, WU Liang, JIANG Bin, LIU Wen-jun, YANG Qin, SONG Jiang-feng, HUANG Guang-sheng, ZHANG Ding-fei, PAN Fu-sheng. Effects of texture and discharge products on the discharge performance of Mg anodes for Mg air batteries [J]. Journal of the Electrochemical Society, 2020, 167: 130528.

[31] LIU Xuan, XUE Ji-lai, LIU Shi-ze. Discharge and corrosion behaviors of the $\alpha$-Mg and $\beta$-Li based Mg alloys for Mg−air batteries at different current densities [J]. Materials & Design, 2018, 16: 138−146.

[32] GU Xiong-jie, CHENG Wei-Li, CHENG Shi-ming, YU Hui, WANG Zhi-feng, WANG Hong-xia, WANG Li-fei. Discharge behavior of Mg–Sn–Zn–Ag alloys with different Sn contents as anodes for Mg−air batteries [J]. Journal of the Electrochemical Society, 2020, 167: 020501.

[33] DONG Xiao-yang, WANG Jin-xing, YANG, Jing-dong, WANG Xiao, ZHU Ling, ZENG Wen, WANG Jing-feng, PAN Fu-sheng. $CuMnO_2$ nanoflakes as cathode catalyst for oxygen reduction reaction in magnesium-air battery [J]. Journal of the Electrochemical Society, 2021, 168: 100502.

[34] LI Chun-sheng, SUN Yan, LAI Wei-hong, WANG Jia-zhao, CHOU Shu-lei. Ultrafine $Mn_3O_4$ nanowires/three-dimensional graphene/single-walled carbon nanotube composites: superior electrocatalysts for oxygen reduction and enhanced Mg/air batteries [J]. ACS Applied Materials & Interfaces, 2016, 8: 27710−27719

[35] DENG Min, WANG Lin-qian, HÖCHE D, LAMAKA S V, JIANG Ping-li, SNIHIROVA D, SCHARNAGL N, ZHELUDKEVICH M L. Ca/In micro alloying as a novel strategy to simultaneously enhance power and energy density of primary Mg−air batteries from anode aspect [J]. Journal of Power Sources, 2020, 472: 228528.

[36] LI Jia-run, WAN Kai, JIANG Quan-tong, SUN Hu-yuan, LI Yan-tao, HOU Bao-rong, ZHU Li-wei, LIU Min. Corrosion and discharge behaviors of Mg−Al−Zn and Mg−Al−Zn−In alloys as anode materials [J]. Metals, 2016, 6: 65.

[37] IKEUBA A I, KOU Fu-jun, DUAN Hao-wei, ZHANG Bo, WANG Jian-qiu, HAN En-hou, KE Wei. Understanding the electrochemical behavior of bulk-synthesized $MgZn_2$ intermetallic compound in aqueous NaCl solutions as a function of pH [J]. Journal of Solid State Electrochemistry, 2019, 23: 1165−1177.

[38] HAN J, OGLE K. Dealloying of $MgZn_2$ intermetallic in slightly alkaline chloride electrolyte and its significance in corrosion resistance [J]. Journal of the Electrochemical Society, 2017, 164: C952−C961.

[39] BI Guang-li, LI Yuan-dong, ZHANG Shi-jun, ZHANG Jian-bin, MA Ying, HAO Yuan. Microstructure, mechanical and corrosion properties of Mg−2Dy−*x*Zn (*x*=0, 0.1, 0.5 and 1 at.%) alloys [J]. Journal of Magnesium and Alloys, 2014, 2: 64−71.

[40] DARGUSCH M S, SHI Zhi-ming, ZHU Han-liang, ATRENS A, SONG Guang-ling. Microstructure modification and corrosion resistance enhancement of die-cast Mg−Al−Re alloy by Sr alloying [J]. Journal of Magnesium and Alloys, 2021, 9: 950−963.

[41] ZHANG Tao, SHAO Ya-wei, MENG Guo-zhe, CUI Zhong-yu, WANG Fu-hui. Corrosion of hot extrusion AZ91 magnesium alloy. I: Relation between the microstructure and corrosion behavior [J]. Corrosion Science, 2011, 53: 1960−1968.

[42] GONG Chang-wei, HE Xin-ze, FANG Da-qing, LIU Bao-sheng, YAN Xue. Effect of second phases on discharge properties and corrosion behaviors of the Mg−Ca−Zn anodes for primary Mg−air batteries [J]. Journal of Alloys and Compounds, 2021, 861: 158493.

# Mg−Zn−Mn−Nd 合金作为一次镁空气电池阳极的腐蚀和放电行为

丁德渝，杜宇航，唐梅芳，宋 波，郭 宁，张红菊，郭胜锋

西南大学 材料与能源学院 分析与测试中心，重庆 400715

**摘 要**：利用金相显微镜、X 射线衍射仪、带有能谱仪的扫描电镜、电化学测试及恒电流放电测试对挤压态及固溶时效态 Mg−6Zn−Mn−*x*Nd (ZM61, *x*=0, 0.2, 0.6, 0.8, 1.0, 质量分数，%)合金微观结构、耐腐蚀性能及放电性能进行表征。结果表明，Nd 的微合金化能促进 ZM61 合金晶粒细化，挤压态及固溶时效态 ZM61−0.6Nd 合金在所有合金中具有最为优异的耐腐蚀性能及放电性能；然而，热处理却降低挤压态合金的综合性能。其中，挤压态 ZM61−0.6Nd 合金的腐蚀电流密度为 $1.611\times10^{-5}$ A/cm$^2$，在电流密度为 1 和 10 mA/cm$^2$ 放电 24 h 的放电电位分别为−1.517 V 和−1.336 V (vs SCE)，其阳极利用率约 36%，在所有研究合金中具有最好的综合性能。分析认为，挤压态 ZM61−0.6Nd 合金良好的放电性能可归因于镁合金耐腐蚀性能的提升及放电产物的开裂效应。

**关键词**：Mg−6Zn−Mn 合金；Nd 添加；镁空气电池；自腐蚀；放电性能

**(Edited by Bing YANG)**